

A Solid-State Maxwell Demon

to appear in *Foundations of Physics* October 2002

D.P. Sheehan*, A.R. Putnam* and J.H. Wright†

* Department of Physics

† Department of Mathematics and Computer Science

University of San Diego, San Diego, CA 92110

619-260-4095, FAX: 619-260-2303

dsheehan@sandiego.edu

Abstract

A laboratory-testable, solid-state Maxwell demon is proposed that utilizes the electric field energy of an open-gap p-n junction. Numerical results from a commercial semiconductor device simulator (Silvaco International – Atlas) verify primary results from a 1-D analytic model. Present day fabrication techniques appear adequate for laboratory tests of principle.

Key Words: second law, nonequilibrium, thermodynamics, nanotechnology, Maxwell demon

1 Introduction

Over the last ten years, an unprecedented number of challenges have been leveled against the absolute status of the second law of thermodynamics. During this period, roughly 40 papers have appeared in the general literature [e.g., 1-20], representing more than a dozen distinct challenges; the publication rate is increasing. Recently, for the first time, a major scientific press has commissioned a monograph on the the subject [21] and a first international conference has been convened to resolve these challenges [22].

Second law challenges are often referred to as Maxwell demons, both to honor the seminal work by J.C. Maxwell [23], and to defend against the jejune stigma often attached to them. The original Maxwell demon [24] is a hypothetical microscopic, sentient creature who, through skillful sorting of individual molecules across a gated partition, is able to create artificial temperature or pressure gradients by which work can be performed at the expense of heat from a heat bath and in violation of the second law. It was realized early on that natural, nonsentient processes can also sort molecules to achieve similar results [25].

The genealogy of the Maxwell demon thus split into those that relied on sentient processes (e.g., intelligent active measurement, calculation, or microscopic manipulation), and those that did not. The former line has largely died out owing to advances in information theory [26], but the latter survived and now poses the most serious threat to the absolute status of the second law.

The present paper is concerned with a new nonsentient solid-state Maxwell demon. It is based on the cyclic electromechanical discharging and thermal recharging of the electrostatic potential energy inherent in the depletion region of a standard solid-state p-n junction. Essentially, it is a thermally-rechargeable capacitor which, in this incarnation, is used to power a linear electrostatic motor. The initial impetus to explore such devices was given in 1995 by J. Bowles, who noted that solid state and plasma physics are close cousins; hence there should be solid-state analogs to the previously proposed plasma paradoxes [1-3].

This challenge is the fifth in a more general class of recent challenges [8], spanning plasma (two challenges [1-3]), chemical [4,5], gravitational [6,7], and (now) solid-state physics. This class is distinguished in that each member utilizes a macroscopic, naturally-occurring, steady-state potential gradient (chemical, electrostatic, gravitational) by which particle flow down the gradient is used to extract work from the system, while at the same time return particle flow is maintained by thermal energy. These macroscopic potential gradients effectively allow the accumulation of potential energy (either in the form of gaseous pressure gradients or electric fields) that can be released to perform macroscopic work. Inasmuch as these gradients occur at equilibrium, their attendant potential energies are thermally generated. By this it is meant that the potential energy arises and is maintained from the collective behavior of many ($\mathcal{N} \gg 1$) microscopic particles in thermal motion (e.g., atoms, ions, electrons). Since a thermal generation - work - thermal regeneration cycle can be established and run indefinitely for each system (when surrounded by an infinite heat bath), this implies that heat can be converted solely into work – in violation of the second law. Also, surprisingly, in several of these systems (both in equilibrium and nonequilibrium configurations) particle potential energies can substantially exceed average particle thermal kinetic energies, sometimes by more than an order of magnitude [1-3, 6,7].

As for the four others currently in its class, this solid-state challenge appears immune to standard second law defenses. Also, as for the others, it is concrete rather than abstract; that is, it has a definite physical form and is based on well-defined, experimentally verified physical processes. This is in contrast with other recent (abstract) challenges that propose generic mechanisms, but which do not offer concrete physical embodiments [9-18].

The previous four challenges in this class have been corroborated by laboratory experiments that verify their underlying physical processes. This is not to claim that any of these experiments actually violated the second law; in fact, the entropy generated by the apparatus required to maintain the experimental conditions for each system's negentropic process (e.g., heaters/coolers, vacuum pumps) was always greater than the

theoretical maximum reduction in entropy which could be achieved by the negentropic process itself. These four previous challenges do claim, however, that were the thermodynamic state of the universe identical to those for which the challenges were posed – thus obviating the need for supporting apparatus – then the second law would be violable.

The present solid-state challenge differs from these previous challenges in one important respect. Whereas previous challenges are cases for the *potential violability* of the second law, given suitable thermodynamic regimes, they offer no practical hope of *actual violation* under everyday terrestrial conditions. The present challenge, on the other hand, makes positive claims on both. Whereas previous challenges are viable only under extreme thermodynamic conditions (e.g., high temperatures ($T \geq 1000\text{K}$) or low pressure ($P \leq 1$ Torr)), the present solid-state challenge is viable at room temperature and pressure and does not require ancillary entropy-generating apparatus. As such, the present challenge appears to be the first to propose both the second law's *potential violability* and its *actual violation* under everyday thermodynamic conditions.

This paper is organized as follows. In Section 2.1 the physics of p-n junctions underlying the solid-state Maxwell demon is introduced and developed via a one-dimensional analytical model. In Section 2.2, numerical results from a commercial semiconductor device simulator (Silvaco International, Atlas) are presented and shown to agree with the 1-D model. In Section 3, a linear electrostatic motor is introduced as the basis of a Maxwell demon. It is substantiated three ways: via a 1-D analytical model, by analogy with an R-C network, and through 2-D numerical simulations. In Section 4, the Maxwell demon is shown to be viable within a broad range of realistic physical parameters. Prospects for near-term laboratory experiments are discussed.

2 Open-Gap P-N Junctions

2.1 One-Dimensional Model

The present challenge is based on the physics of the standard p-n junction diode. At equilibrium, the depletion region of a diode represents a minimum free energy state in which bulk electrostatic and diffusive forces are balanced. It follows that when individual n- and p- materials are joined, there is a transient current and energy release as a depletion region forms and equilibrium is attained. Typical depletion regions are narrow, ranging from $10\mu\text{m}$ for lightly-doped semiconductor to $0.01\mu\text{m}$ for heavily-doped ones. Although these distances are small, the broadest depletion regions have scale lengths visible to the naked eye and the narrowest are two orders of magnitude larger than atoms; therefore, they will be considered macroscopic. They are large enough to interact with some present-day and many envisioned micro- and nano-scale devices [27-29]. The thermally-generated electrostatic potential energy of the depletion region fuels the challenge.

Consider a p-n device (Fig. 1) consisting of two symmetric horseshoe-shaped pieces of n- and p-semiconductor facing one another. At Junction I (J-I), the n- and p-regions are physically connected, while at Junction II (J-II) there is a vacuum gap whose width (x_g) is small compared to the scale lengths of either the depletion region (x_{dr}) or the overall device (x_{dev}); that is, $x_g \ll x_{dr} \sim x_{dev}$. Let the n- and p-regions be uniformly doped and let the doping be below that at which heavy-doping effects such as band gap narrowing are appreciable. The p-n junction is taken to be a step junction; diffusion of donor (D) and acceptor (A) impurities is negligible; the depletion approximation holds; impurities are completely ionized; the semiconductor dielectric is linear; and the system operates at room temperature. For a silicon device as in Fig. 1, representative physical parameters meeting the above conditions are: $N_A = N_D = 10^{21} \text{ m}^{-3}$, $x_{dev} = 10^{-6} \text{ m}$ on a side, $x_{dr} = 1.2 \times 10^{-6} \text{ m}$, and $x_g = 3 \times 10^{-8} \text{ m}$. This dopant concentration results in a built-in potential of $V_{bi} \simeq 0.6 \text{ V}$. For the discussion to follow, the p-n device (Fig. 1) with these parameters

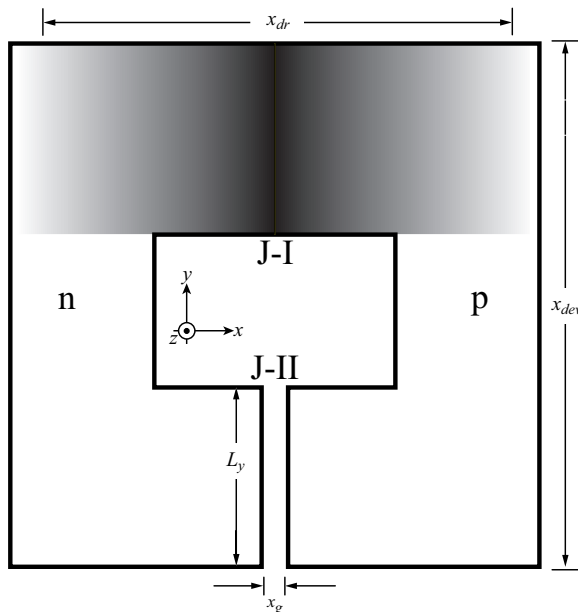


Figure 1: *Standard device* with Junctions I and II and physical dimensions and standard coordinates indicated. Depletion region at Junction I is shaded.

will be called the *standard device*.

Standard one-dimensional formulae have been used to estimate V_{bi} and x_{dr} [30,31]:

$$V_{bi} = \frac{kT}{q} \ln\left(\frac{N_A N_D}{n_i^2}\right) \quad (1)$$

and

$$x_{dr} = \left[\frac{2\kappa\epsilon_o V_{bi} (N_A + N_D)}{q N_A N_D} \right]^{\frac{1}{2}} \quad (2)$$

Here kT is the thermal energy; q is an electronic charge; n_i is the intrinsic carrier concentration of silicon ($n_i \simeq 1.2 \times 10^{16} \text{ m}^{-3}$ at 300K); ϵ_o is the permittivity of free space; and $\kappa = 11.8$ is the dielectric constant for silicon.

In Figure 2, the energy (\mathcal{E}), space charge density (ρ), and electric field (\mathbf{E}) are depicted versus horizontal position (x) through J-I and J-II. There are several important differences between the two junctions. The most noticeable is that, while physical properties vary continuously with position across the J-I region, there are marked discontinuities for J-II. These are due to the inability of electrons to jump the vacuum gap (x_g). This restricts the diffusion of charge carriers that would otherwise spatially smooth the physical properties. As a result, Junction II suffers discontinuities in energies, voltages and space charge. Because the J-II gap is narrow and the built-in potential is discontinuous, there can be large electric fields there, more than an order of magnitude greater than in the J-I depletion region. Treating the gap one-dimensionally, the J-II electric field is uniform, with $|\mathbf{E}_{\text{J-II}}| \simeq \frac{V_{bi}}{x_g}$, while in the J-I bulk material it has a triangular profile, with average magnitude $|\mathbf{E}_{\text{J-I}}| \sim \frac{V_{bi}}{x_{dr}}$. The ratio of the electric field strength in the J-II gap to that in the middle

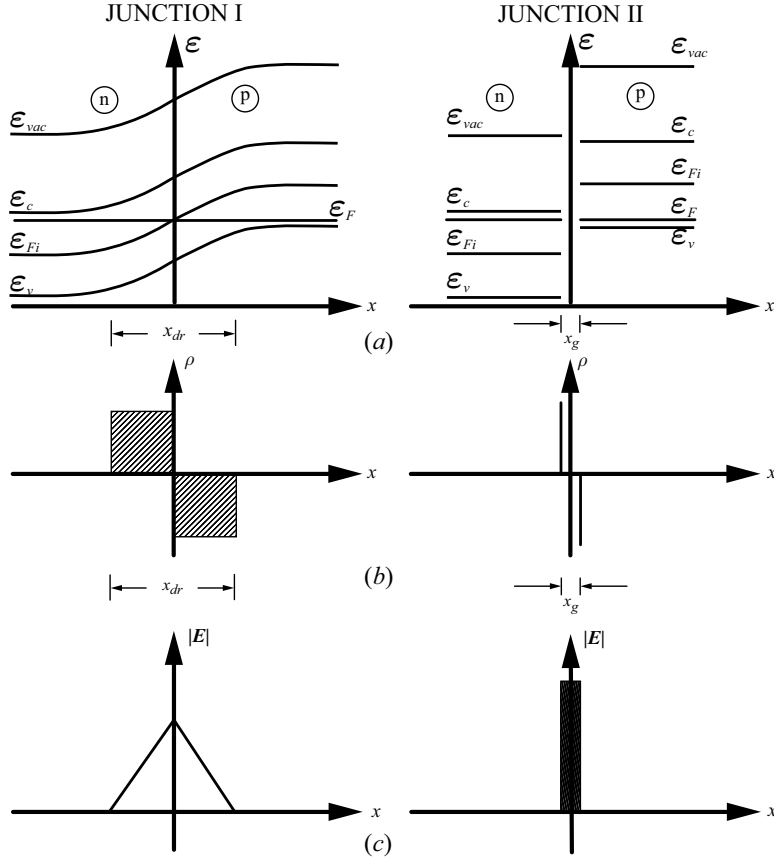


Figure 2: Physical characteristics versus position x through Junctions I and II. Left ($x < 0$) and right ($x > 0$) sides of each graph corresponds to n- and p-regions, respectively. (a) Energy levels for vacuum (\mathcal{E}_{vac}), conduction band edge (\mathcal{E}_c), intrinsic Fermi level (\mathcal{E}_{Fi}), Fermi level (\mathcal{E}_F), valence band edge (\mathcal{E}_v). (b) Charge density (ρ). (c) Electric field magnitude ($|\mathbf{E}|$) Note that vertical scales for \mathbf{E} are different for J-I and J-II ($|\mathbf{E}_{J-II}| \gg |\mathbf{E}_{J-I}|$).

of the J-I depletion region scales as $\frac{E_{J-II}}{E_{J-I}} \sim \frac{x_{dr}}{x_g} \gg 1$. For the *standard device*, the average value of the field strength is $|E_I| \sim \frac{0.6V}{1.2 \times 10^{-6}m} \simeq 5 \times 10^5$ V/m and $|E_{II}| \sim \frac{0.6V}{3 \times 10^{-8}m} \sim 2 \times 10^7$ V/m, rendering $\frac{E_{J-II}}{E_{J-I}} \sim 40$.

Now let a switch bridge the J-II gap, physically connecting the entire facing surfaces of the n- and p- regions. For the present discussion, let the switching element be simply a slab of intrinsic semiconductor inserted into the J-II gap. If the current transmission through the slab is good (that is, its effective resistance and junction potentials are small), then when equilibrium is reached, the physical characteristics of J-II will be approximately those of J-I, as depicted in Fig. 2.

Theoretical limits to the energy released from J-II during its transition from an open- to a closed-switch configuration can be estimated from the total electrostatic energy \mathcal{E}_{es} inherent to the J-II junction. Let $\Delta\mathcal{E}_{es}(J-II) = [\mathcal{E}_{es}(J-II, open) - \mathcal{E}_{es}(J-II, closed)]$ be the difference in electrostatic energy in J-II between its closed- and opened-switch equilibrium configurations (Fig. 2). Within the 1-D model constraints, this can be shown to be roughly:

$$\Delta\mathcal{E}_{es}(J-II) \simeq \frac{\epsilon_o}{2} \left[\frac{x_{dr} kT}{q} \ln\left(\frac{N_A N_D}{n_i^2}\right) \right]^2 \cdot \left[\frac{1}{x_g} - \frac{1}{3} \frac{\kappa}{x_{dr}} \right], \quad (3)$$

By eliminating V_{bi} and x_{dr} with Eqs. (1 and 2) and using $N_A = N_D \equiv N$, Eq. (3) can be recast into:

$$\Delta\mathcal{E}_{es}(J-II) \simeq \frac{16\kappa\epsilon_o^2}{qN} \left\{ \frac{kT}{q} \ln\left[\frac{N}{n_i}\right] \right\}^3 \left\{ \frac{1}{x_g} - \frac{2}{3} \kappa \left(\frac{2\kappa\epsilon_o}{Nq} \left(\frac{kT}{q} \right) \ln\left[\frac{N}{n_i}\right] \right)^{-1/2} \right\} \quad (4)$$

It is evident from Eq. (4) that the device's energy varies strongly with temperature, scaling as $(T)^3$. This is not surprising since primary determinants of the energy are V_{bi} and x_{dr} , both of which originate from thermal processes.

For the *standard device*, Eq. (3) predicts the J-II region contains roughly three times the electrostatic potential energy of the J-I region. Equivalently, the whole p-n device contains twice the energy in its open-gap configuration as it does in its closed-gap configuration and the majority of this excess energy resides in the electric field of the open J-II vacuum gap.

The energy release in closing the J-II gap is essentially equivalent to the discharge of a capacitor. For the *standard device*, Eq. (3) gives the net energy release as $\Delta\mathcal{E}_{es}(J-II) \sim 5.2 \times 10^{-17} \text{J} \sim 320$ eV. When J-II is open, there are about 330 free electronic charges on each gap face (calculable from Gauss' law); when it is switched closed, most of these disperse through and recombine in the J-II bulk. This net flow of charges is due to particle diffusion powered by concentration gradients and to particle drift powered by the large capacitive electric field energy of the open J-II vacuum gap. Thermodynamically, this energy release may be viewed as simply the relaxation of the system from a higher to a lower energy equilibrium state.

The device output power P_{dev} scales as: $P_{dev} \sim \frac{\Delta\mathcal{E}_{es}(J-II)}{\tau_{dis}}$, where τ_{dis} is the characteristic discharging time for the charged open-gap J-II region as it is closed. If τ_{dis} is short, say $\tau_{dis} \simeq 10^{-7} - 10^{-8}$ sec – a value consistent with the size of micron-sized p-n junctions or typical inverse slew rates of micron-sized transistors – then the instantaneous power for a single, switched *standard device* should be roughly $P_{dev} \simeq 0.5 - 5 \times 10^{-9}$ W. Instantaneous power densities for these devices can be large; for the *standard device* it is on the order of $\mathcal{P}_{dev} = \frac{P_{dev}}{(10^{-6}m)^3} \sim 0.5 - 5 \times 10^9 \text{ Wm}^{-3}$.

2.2 Two-Dimensional Simulation

Two-dimensional numerical simulations of this system were performed using Silvaco International's semiconductor Device Simulation Software [Atlas (S-Pisces, Giga)]. Junctions were modeled as abrupt and the physical parameters for charge carriers were generic. Output from the simulations were the two-dimensional,

steady-state, simultaneous solutions to the Poisson, continuity, and force equations, using the Shockley-Read-Hall recombination model. This 2-D simulator has significant phenomenological character, but as will be shown shortly, there is good agreement between its physical predictions and those of the 1-D analytic model, which is far less phenomenological.

Devices identical to and similar to the *standard device* were studied. Over a wide range of experimental parameters ($10^{17} \leq N_{A,D} \leq 10^{26} \text{m}^{-3}$; $10^{-8} \leq x_g \leq 3 \times 10^{-7} \text{m}$), the two-dimensional numerical simulations showed good agreement with the primary findings of the 1-D analytic model, most significantly that much larger electric fields reside in the J-II vacuum gap than in the J-I junction, and that significant electrostatic energy is both stored in the J-II region and is released upon switching. Their differences can be traced primarily to the unrealistic discontinuities in physical parameters in the 1-D model, which were smoothed by the more realistic 2-D simulator.

In Figure 3, the electric field magnitude is shown for three related variations of the *standard device*. Figure 3a (hereafter, Case 1) depicts the electric field for the *standard device*, with the J-II gap closed. As expected, the electric fields are modest ($|\mathbf{E}| \leq 10^6 \text{ V/m}$) and are centered on the depletion regions, which, as predicted in the 1-D model, extend over the length of the device. The field structure demonstrates perfect symmetry with respect to its horizontal mirror plane and rough mirror symmetry with respect to its vertical mirror plane. Perfect horizontal mirror symmetry is demanded by the Curie/von Neumann principle and the imperfect vertical mirror symmetry is due to the differences in the physical properties of the charge carriers. (With proper dopant concentration profiles, vertical symmetry should also be possible.)

Figure 3b (Case 2) depicts the electric field magnitude for the *standard device*. While the electric fields in the J-I depletion regions of Cases 1 and 2 are similar, in the J-II regions they are significantly different. The J-II electric field in Case 2 is $E \sim 7 \times 10^6 \text{ V/m}$ versus an average of $E \sim 5 \times 10^5 \text{ V/m}$ for Case 1. Numerical integration of the electrostatic field energy over the entire region (vacuum and bulk) indicates the total electrostatic energy of Case 2 is roughly 1.5 times that of Case 1. Considering only the J-II region of each device, Case 2 stores roughly twice the electrostatic energy of Case 1. These are within 50% of the energy estimates of the 1-D analytic model. (Fuller discussion of energy will be taken up later.)

Figure 3c depicts Case 3, a configuration intermediate between Cases 1 and 2, and one in which the J-II gap of the *standard device* is 20% bridged at its center by a slab of undoped silicon ($l_x = 300 \text{ \AA}$, $l_y = 600 \text{ \AA}$). As expected, the bridge allows electron-hole transport between the n and p regions, thereby reducing the large fields of Case 1 closer to values of Case 2. The field is attenuated most across the bridge, but in fact, attenuation extends over the entire length of the channel (L_y). The electrostatic energy of Case 3 is intermediate between Cases 1 and 2. The electric fields for all cases are primarily in the x -direction, and especially so for Case 2.

In Figure 4, the mid-channel electric field [32] is plotted versus gap width for Case 2 of the *standard device* (Fig. 3b). Predictions of the 1-D analytic model are compared with results of 2-D numerical simulations [33]. As expected, the magnitude of the J-II electric field varies inversely with the gap width, x_g . The 1-D analytic model overestimates the electric field compared with the 2-D numerical simulation, particularly at small x_g , but this is not surprising since the 1-D model has an unphysical singularity at $x_g = 0$. At small gap widths ($x_g \ll L_y$), the 1-D model predicts the electric field should vary strictly as $\frac{1}{x_g}$, whereas in the 2-D model, the charge carriers in the bulk respond to the high fields, disperse, and thereby moderate them. As a result, the 2-D model consistently renders lower field strengths than the 1-D model. The field strength in the 2-D model saturates at roughly 10^7 V/m , safely below the dielectric strength of silicon. At larger gap widths ($x_g \sim L_y$), the two models display good agreement.

In Figure 5, we display the J-II mid-channel electric field for the *standard device* versus dopant concentration ($N \equiv N_A = N_D$). Values for the 1-D model (estimated as $|\mathbf{E}| = \frac{V_{bi}}{x_g}$ using Eq. (1) and $x_g = 3 \times 10^{-8} \text{m}$)

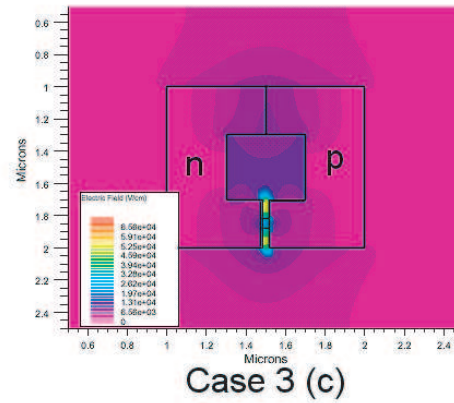
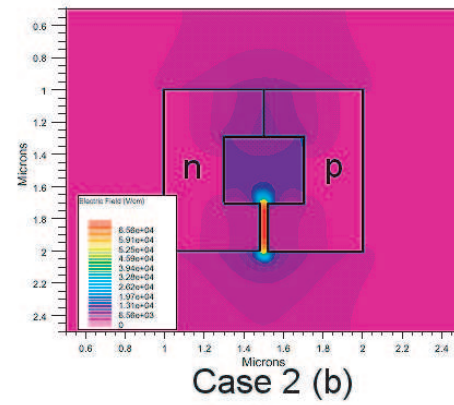
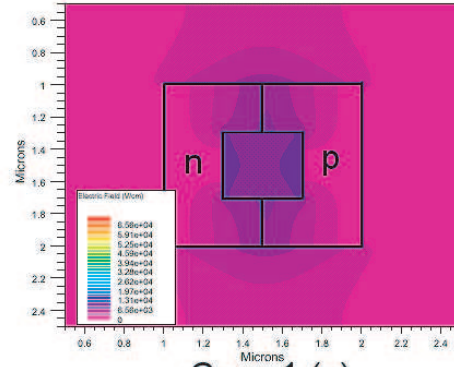


Figure 3: Atlas 2-D numerical simulations of electric field for three related variations of the *standard device*. a) Case 1: *standard device* without J-II gap; b) Case 2: *standard device*; c) Case 3: *standard device* with $300\text{\AA} \times 600\text{\AA}$ undoped silicon piston at gap center.

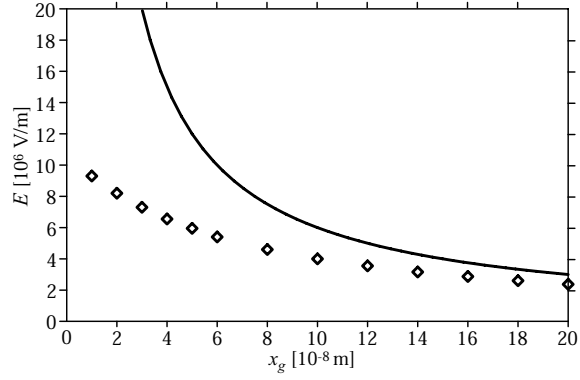


Figure 4: Electric field strength for *standard device* (Fig. 1) versus gap width x_g calculated at geometric center of J-II region for 1-D analytic model (solid line) and 2-D numerical model (open diamonds).

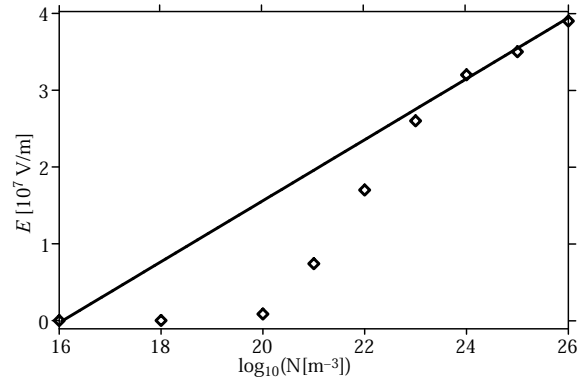


Figure 5: J-II mid-channel electric field for *standard device* versus dopant concentration ($N_A = N_D \equiv N$) for 1-D analytic model (solid line) and 2-D numerical model (open diamonds).

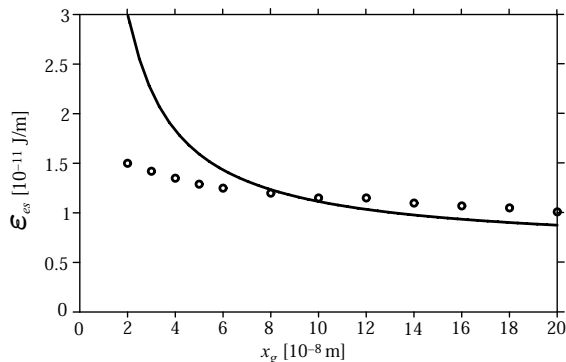


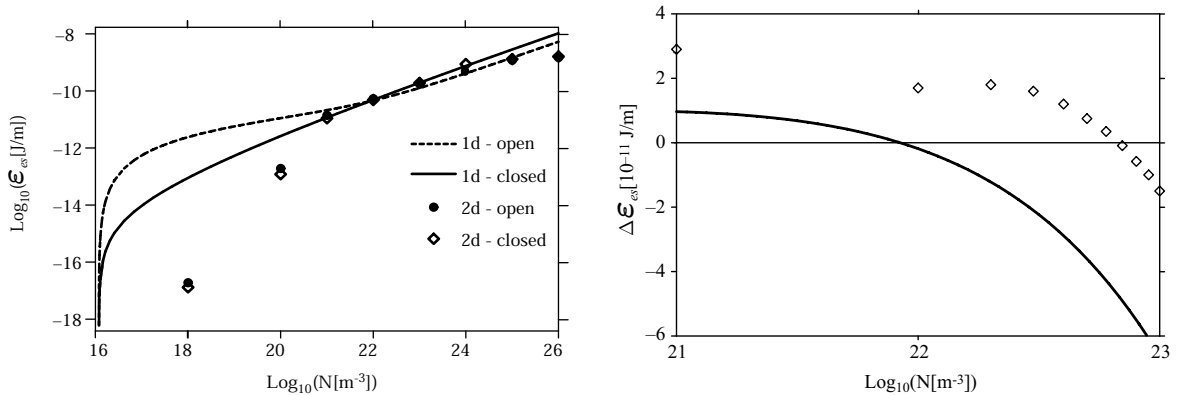
Figure 6: Z-normalized electrostatic potential energy \mathcal{E}_{es} versus gap width (x_g) for *standard device* in 1-D model (solid line) and 2-D model (open circles)

are compared to the results of the 2-D model. Above $N \simeq 10^{23}\text{m}^{-3}$ the two models are in good agreement; below this the agreement worsens. At the density of the *standard device* ($N = 10^{21}\text{m}^{-3}$), the 2-D model predicts an electric field magnitude roughly a factor of 3 less than the 1-D model, in agreement with the results of Fig. 4.

Electrostatic potential energy is stored in the J-I and J-II regions of the device in both the open- and closed-gap configurations. In Figure 6, \mathcal{E}_{es} is plotted versus x_g for the *standard device*, comparing the 1-D and 2-D models. (Note that the energy is normalized here with respect to the z -direction (J/m) so as to conform with the output of the 2-D model.) The total electrostatic energy is the sum of the contributions from the vacuum energy density ($\frac{\epsilon_0 E^2}{2}$) and n-p bulk energy density ($\frac{\kappa \epsilon_0 E^2}{2}$), integrated over their respective regions. In the 1-D model, we take the electric field in the J-II gap to be constant, while in the J-I region it is taken to have a triangular profile as in Fig. 2, with maximum electric field strength of $E_{max} = \frac{2V_{bi}}{x_{dr}}$. For both models, the device energy decreases monotonically with increasing gap width, however their magnitudes and slopes differ due to the differing model assumptions. At small gap widths ($x_g \leq 10^{-7}\text{m}$), the 1-D model predicts greater energy than the 2-D model, owing principally to its vacuum energy, however, at larger gap widths ($x_g \geq 10^{-7}\text{m}$) the energy in the 2-D model's n-p bulk dominates, as will be shown later (Fig. 8). The 1-D model explicitly ignores contributions of energy to the open-gap configuration arising from the p-n bulk semiconductor on either side of the gap. (See Eq. (3).) In the density vicinity of the *standard device* the two models agree to within about 50%.

The stored electrostatic potential energy of the device strongly depends upon the dopant concentration. In Figure 7a, \mathcal{E}_{es} is plotted for the *standard device* versus dopant concentration N , for both open- and closed-gap configurations, comparing 1-D and 2-D models. Above $N = 10^{18}\text{m}^{-3}$ the 1-D model shows roughly constant logarithmic increase in \mathcal{E}_{es} with increasing N , while the 2-D model shows a roughly constant logarithmic increase up to about $N \simeq 10^{21}\text{m}^{-3}$, at which point \mathcal{E}_{es} begins to flatten out and saturate for both open- and closed-gap configurations.

Both models display a crossover in energy between the open-gap and closed-gap configuration (See Fig. 3) above the dopant concentration of the *standard device* ($N = 10^{21}\text{m}^{-3}$). These are visualized in Fig. 7b, in which $\Delta\mathcal{E}_{es} = [\mathcal{E}_{es}(open) - \mathcal{E}_{es}(closed)]$ is plotted versus N . The crossover density N_{cross} is where $\Delta\mathcal{E}_{es}$ reverses sign. In the 2-D model the energy crossover occurs at $N_{cross} \simeq 7 \times 10^{22}\text{m}^{-3}$, while in the 1-D model it occurs at $N_{cross} = 8 \times 10^{21}\text{m}^{-3}$. Above N_{cross} the closed-gap configuration is more energetic than the



(a) Comparison of 1-D and 2-D models.

(b) Energy difference $\Delta\mathcal{E}_{es}$ versus N for 1-D model (line) and 2-D model (open diamonds). Crossover density N_{cross} indicated by zero crossing.

Figure 7: Z-normalized electrostatic energy \mathcal{E}_{es} versus dopant concentration (N) for *standard device* for open- and closed-gap configurations.

open-gap one. As a result, above N_{cross} one cannot expect to extract energy by closing the J-II gap. The *standard device* operates at $N = 10^{21} \text{m}^{-3}$, which is a factor of 8 below the 1-D crossover and a factor of 70 below the 2-D crossover density. If the gap is not fully closed, but bridged, as in Case 3 (Fig. 3c), then the 2-D model renders a lower crossover density, one much closer to the one given by the 1-D model. Specifically, for a 20% bridge at mid-channel of the *standard device* (Case 3, Fig. 3c), the revised 2-D crossover density is $N_{cross} \simeq 10^{22} \text{m}^{-3}$.

Energy release due to gap closing can be made continuous. Let a tightly fitting rectangular slab of silicon be inserted into the gap, thereby allowing the transport of charge between the separated n- and p-regions and the relaxation of the J-II region into an equilibrium state like J-I (Fig. 2). Figure 8 displays the electrostatic energy of the *standard device* (\mathcal{E}_{es}) versus bridging fraction by a slab of undoped silicon ($x_g = 300 \text{\AA} \times 3000 \text{\AA} = L_y$). Here, 0% bridging corresponds to a completely open configuration and 100% bridging corresponds to a completely closed configuration. (Additional simulations show that the substitution of undoped silicon by n- and p-doped silicon makes little difference, probably owing to the thinness of the bridge.) In addition to the vacuum, p-n bulk and total system energies, the electrostatic energy of the silicon bridge itself is shown. For a *standard device* of $(1 \mu\text{m})^3$ total volume, the 2-D model predicts $\Delta\mathcal{E}_{es}$ to be roughly $7 \times 10^{-18} \text{J} \sim 45 \text{ eV}$ per gap closure, a factor of about 7 times less than is predicted by the 1-D model (Fig. 8).

As expected, the total system, vacuum, and bulk energies decrease as the silicon is inserted; the silicon bridge energy increases slightly with its insertion. At full insertion, the system's energy is partitioned between bulk, vacuum and piston energy in a ratio of roughly 6 : 1 : 0.25. These data suggest that for minimal investment in piston energy, roughly 10 times more energy is released in the device as a whole. The 2-D simulations indicate a faster-than-linear decrease in system energy with bridging fraction. This can be explained by the natural transport of charge into the bulk ahead of the silicon slab.

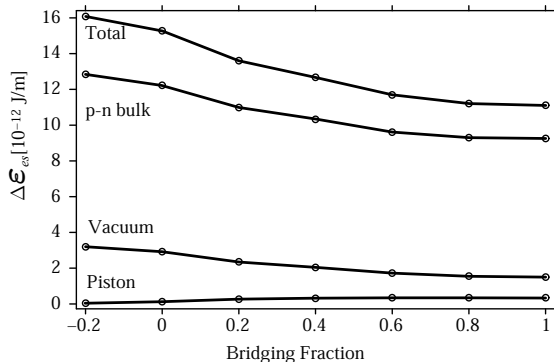


Figure 8: Z-normalized electrostatic energies \mathcal{E}_{es} versus gap bridging fraction by undoped silicon slab.

In summary, the 1-D analytic and the 2-D numerical models agree well with respect to the basic physics of the *standard device*. This is encouraging, especially given the strong simplifying assumptions inherent in the 1-D model.

3 Linear Electrostatic Motor

The 1-D analytic and the 2-D numerical models above verify that significant electrostatic potential energy resides in the J-II region of the *standard device* and that it can be released when the device is switched from an open to a closed configuration. Both configurations (Cases 1 and 2 in Fig. 3) represent equilibrium states; that is, these are states to which the device relaxes when left alone in a heat bath. Their energies are different because of their differing boundary conditions, specifically in the J-II gap, which frustrates the diffusive transport of electrons and holes between the n- and p-regions. Since each configuration is a state to which the system naturally thermally relaxes, the device may be made to cycle between Cases 1 and 2 simply by opening and closing (bridging) the J-II gap with a piston (as done in Fig. 8). Many energy extraction schemes can be imagined [34]. Here we consider one that can be rigorously analysed: a linear electrostatic motor.

The motor consists of a dielectric piston in the J-II gap which is propelled by a self-generated, electrostatic potential energy minimum (pulse). This electrostatic pulse propagates back and forth through the channel, carrying the piston with it. The piston itself creates the potential energy minimum in which it rides by electrically bridging the J-II gap locally. The free energy that drives the piston resides in the gap electric field; its thermal origin was discussed earlier (See Eq. (4)). In essence, the piston perpetually ‘surfs’ an electrostatic wave that it itself creates. As will be shown, the piston can surf under load (thus performing work) in the presence of realistic levels of friction and Ohmic dissipation. In accord with the first law of thermodynamics, the net work performed must come from the surrounding heat bath; however, if the first law is satisfied, then the second law is compromised.

3.1 1-D Analytic Model

Consider a dielectric slab piston situated outside a charged parallel plate capacitor, as in Figure 9a. Let its motion be frictionless. It is well known that the dielectric slab will experience a force drawing it between

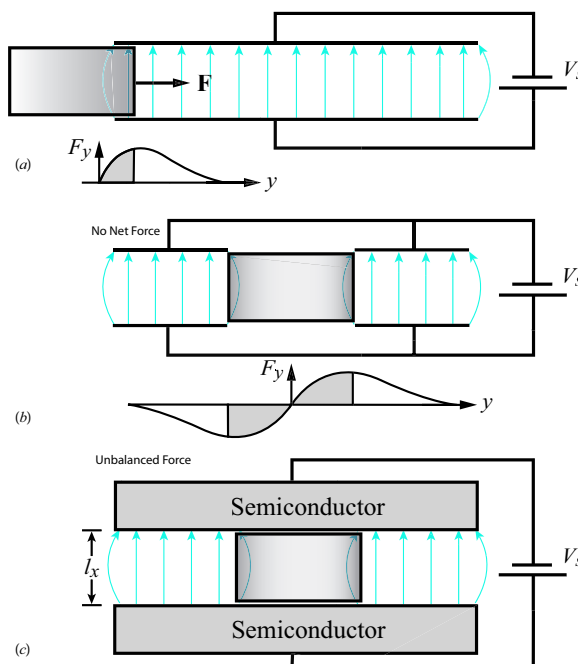


Figure 9: Dielectric interacting with capacitors, with accompanying force versus displacement graphs. a) Dielectric piston is drawn into charged capacitor via $[(\mathbf{p} \cdot \nabla)\mathbf{E}]_y$ force. b) Dielectric piston situated equidistantly between two equivalent capacitors in an unstable equilibrium; unbalanced force in direction of displacement. c) Linear electrostatic motor (rail gun): semiconducting dielectric piston in unstable equilibrium between semiconducting capacitor plates.

the capacitor plates; this is indicated by the accompanying force diagram, which gives the force density experienced by the dielectric at a given horizontal position. The force can be calculated either by integration of the $(\mathbf{p} \cdot \nabla)\mathbf{E}$ force over the piston volume, or equivalently, by invoking the principle of virtual work since the total energy of the the piston-capacitor system is reduced as the slab enters the stronger field region between the plates. As the force diagram indicates (Fig. 9a), the piston experiences a force only so long as it is in the inhomogeneous field near the end of the capacitor. Specifically, the y -force (F_y) requires gradients in the y -component of the electric field; i.e., $[(\mathbf{p} \cdot \nabla)\mathbf{E}]_y = F_y = (p_x \frac{\partial}{\partial x} + p_y \frac{\partial}{\partial y})E_y$. (The method of virtual work is as straightforward to apply as the $(\mathbf{p} \cdot \nabla)\mathbf{E}$ method is notoriously difficult. The latter might be more satisfying, however, for nonlinear, time-dependent systems with complex boundary conditions such as this, the former has the advantages of allowing analytic tractability and closed-form solutions.)

Now let the stationary dielectric piston be situated symmetrically between two identical capacitors (Fig. 9b). Here the net force on the piston is zero and it rests at equilibrium. However, as the accompanying force diagram indicates, this equilibrium is unstable since any infinitesimal y -displacement increases the net force on the piston in the direction of its displacement, while simultaneously reducing the net force in the opposite direction. As a result, the piston will accelerate in the direction of its initial displacement.

Next, consider Figure 9c, which depicts a semiconducting dielectric piston at rest, situated between two semiconductor capacitor plates. (Compare this to Case 3 in Fig. 3.) The semiconducting dielectric

piston allows charge transport between the plates, and so it locally reduces the electric field in and around the piston; thus, the piston sees more intense fields to either side. Essentially, it is in the same unstable equilibrium depicted in Fig. 9b. If displaced, it will accelerate in the direction of its displacement.

From the principle of virtual work [35], one can write the frictionless electrostatic acceleration (a_{es}) of the piston (mass density ρ ; physical dimensions l_x, l_y, l_z ; dielectric constant ϵ) inside a long parallel plate capacitor as

$$a_{es} \simeq \frac{\epsilon - \epsilon_o}{2l_y\rho}(E_1^2 - E_2^2) = \frac{\epsilon - \epsilon_o}{2\rho l_y l_x^2} V_s^2 (\alpha_1^2 - \alpha_2^2), \quad (5)$$

where E_1 and E_2 are the electric field strengths at the ends of the piston and $\alpha_{1,2} = \frac{E_{1,2}}{E_o}$, where $E_o = \frac{V_s}{l_x}$ is the strength of the undisturbed electric field far from the piston.

If the piston is at rest, then by symmetry $E_1 = E_2$, and there is no acceleration, but if the piston is displaced, then $E_1 \neq E_2$ and the piston accelerates in the direction of motion. In the frictionless case, the piston is unstable to any displacement. In essence, this motor is an electrostatic rail gun, the electrostatic analog of the well-known magnetic rail gun [36].

We note that $a_{es} \neq 0$ only for the case of both a semiconductor capacitor and a semiconductor piston; if either the piston or the capacitor plates are perfectly conducting or perfectly insulating, then $a_{es} = 0$. (Analogous failures occur for the magnetic rail gun.) If the capacitor plates are perfect conductors (approximated by metallic plates), then the plate surfaces must be equipotentials, in which case there cannot be a net electric field difference between the front and back ends of the piston ($E_1 - E_2 = 0$), therefore $a_{es} = 0$. On the other hand, if the plates are perfect insulators, then their surface charges are immobile and the electric field remains the same throughout the capacitor despite any displacement of the piston and again $E_1 - E_2 = 0$ [37]. Conversely, if the piston is a perfect conductor, its surfaces must be equipotentials so the electric field at the front and back must be the same ($E_1 - E_2 = 0$), or alternatively, one can say that, as a conductor, electric fields cannot penetrate into the piston interior so as to apply the $[(\mathbf{p} \cdot \nabla)\mathbf{E}]_y$ force, and again there can be no net force exerted on it. Finally, if the piston is an insulator, then charge residing on the capacitor plates cannot flow through it so as to diminish the electric field; again, $E_1 - E_2 = 0$. Thus, it is only when both the piston and the plates have finite, non-zero conductivities that they can act as an electrostatic motor.

Assuming the piston to be a semiconducting ($0 < \sigma < \infty$) dielectric (ϵ), then using Ohm's law ($\mathbf{J} = \sigma\mathbf{E}$), the continuity equation ($\nabla \cdot \mathbf{J} = -\frac{\partial \rho}{\partial t}$), and Gauss' law ($\nabla \cdot \mathbf{E} = \frac{\rho}{\epsilon_o}$), one can describe the acceleration of the piston in terms of its electromechanical properties as it locally shorts out the electric field in the channel through which it passes:

$$a_{es} = \frac{\epsilon - \epsilon_o}{2\rho l_y} \left[\frac{V_s}{l_x} \right]^2 \exp[-\beta\eta] \{1 - \exp[-\eta]\} = \frac{\epsilon - \epsilon_o}{2\rho l_y} E_o^2 \exp[-\beta\eta] \{1 - \exp[-\eta]\} \quad (6)$$

Here $\eta = \frac{2\sigma l_y}{\epsilon v_y}$, v_y is the velocity of the piston, and β is a phenomenological constant that is a measure of how far ahead of the moving piston the electric field is affected. β must be positive to avoid unphysical delta function charge densities. Small β values are evidenced in later 2-D simulations (Fig. 13); here we take $\beta = 0.1$.

Consider a rectangular slab of silicon ($l_x = 300\text{\AA}; l_y = 600\text{\AA}; l_z = 10^4\text{\AA}$, $\sigma = 4 \times 10^{-3}(\Omega m)^{-1}$, $\kappa = 11.8$), hereafter called the *standard piston*). In Figure 10, the *standard piston's* acceleration is plotted versus η for the *standard device*. Curve A represents the frictionless case. In the limits of $v_y \rightarrow 0$ ($\eta \rightarrow \infty$) and $v \rightarrow \infty$ ($\eta \rightarrow 0$), one has $a_{es} \rightarrow 0$, as expected. The former case ($v_y = 0$) has been treated previously (Fig. 9). For $v_y \rightarrow \infty$, the piston moves too quickly for the capacitor's charge to cross the piston and short out the

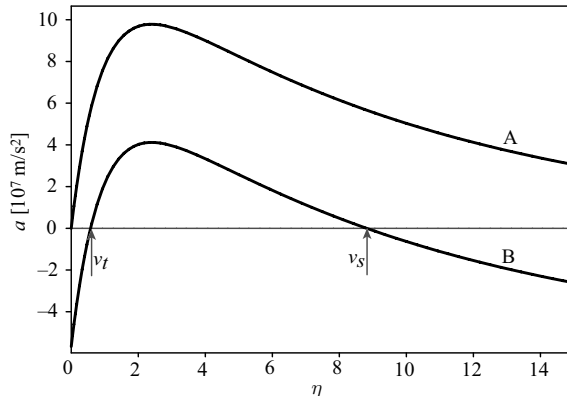


Figure 10: Acceleration of piston a_{es} versus η for *standard device*. Curve A: No friction or load. Curve B: Non-zero friction or load ($a = 5.6 \times 10^7 \text{m/sec}^2$); minimum starting velocity and terminal velocity indicated.

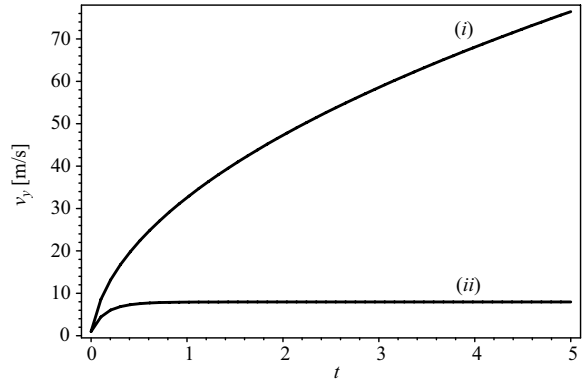
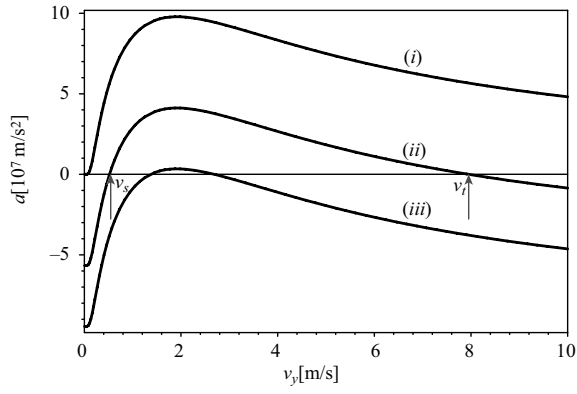
field, so $E_1 - E_2 = 0$ and $a_{es} = 0$. Since σ and v_y are reciprocals in η , this model also predicts, as before, that $a_{es} = 0$ if the piston is perfectly conducting ($\sigma = \infty$) or perfectly insulating ($\sigma = 0$) and, therefore, accelerates only for the semiconductor case.

The form of a_{es} in Eq. (6) is handy for introducing friction on, and loading of, the piston. This model considers loading to be constant over the range of velocities of the piston, with the result that its acceleration curves are simply shifted down by an amount equal to the magnitude of the loading. Thus a non-zero start-up velocity and a bounded terminal velocity are imposed on the piston dynamics. We point out that the negative portion of Curve B to the right of v_s does not signify negative acceleration, but simply indicates values of η for which motion is forbidden.

Numerical integration of Eq. (6), incorporating friction and load resistances, allows investigation of the piston's complex nonlinear dynamics [38]. For example, in Figure 11a, the *standard piston's* velocity is plotted versus time for three values of friction/loading for the *standard device*. Curve (i) corresponds to the unloaded, frictionless piston case; it has no classically-defined terminal velocity. Curve (ii) corresponds to the piston subject to a constant frictional/load acceleration of $5.6 \times 10^7 \text{ m/sec}^2$. In this case, the piston has a terminal velocity of roughly 8 m/sec. Finally, for Curve (iii) ($a = 9.4 \times 10^7 \text{ m/sec}^2$ friction/load), the piston has only a narrow range of velocities for which it has positive acceleration; for greater friction or loading the piston does not begin to move.

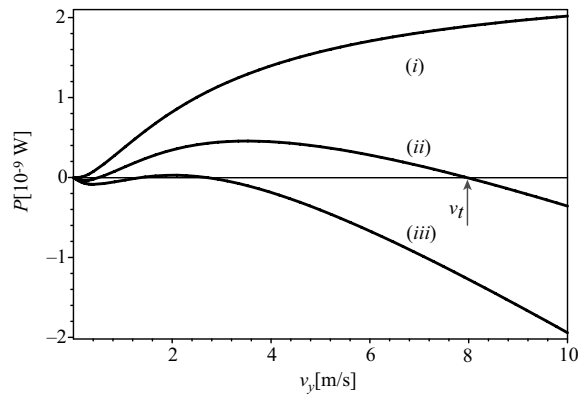
Figure 11b displays v_y versus time for the same three cases as in Fig. 11a. These curves were generated by integrating Eq. (6) via a 4th-order Runge-Kutta scheme, assuming a 1 m/sec start-up velocity for curves (ii) and (iii). In the frictionless case (i), the piston velocity increases monotonically without bound. For the case of moderate friction/loading (ii), the velocity quickly approaches terminal velocity ($\sim 8 \text{ m/sec}$), while for the heavy friction/loading case (iii), the 1 m/sec start-up velocity is insufficient to bring the piston into its positive acceleration regime (Fig. 11a); thus its motion damps out entirely.

Figure 11c plots piston power versus v_y for the previous three cases. In the frictionless case (Curve (i)), power increases monotonically, but is bounded. Cases (ii) and (iii) display local maxima. The power maximum for case (ii) occurs below its terminal velocity, indicating that the most efficient power extraction schemes should use velocity-governed loads, rather than constant loads. Also, notice that case (ii) and (iii) show initially negative excursions, evidence that energy must be supplied to kick-start the piston's motion.



(a) Acceleration versus v_y for three cases: (i) frictionless; (ii) friction/load acceleration $a = 5.6 \times 10^7 \text{ m/sec}^2$; and (iii) friction/load acceleration $a = 9.4 \times 10^7 \text{ m/sec}^2$.

(b) Velocity versus time for cases (i) and (ii) above; case (iii) absent for lack of sufficient start-up velocity.



(c) Piston power versus v_y for cases (i) - (iii) above.

Figure 11: Piston dynamics for *standard device*.

There are three characteristic time scales pertinent to the operation of the *standard device*: (i) the plate discharge time along the piston ($\tau_{dis} \simeq \frac{l_y}{v_y}$); (ii) the recharging time for the plates (τ_{rec}); and (iii) the period of oscillation of the piston in the channel ($\tau_{osc} \simeq \frac{2L_y}{v_y}$), where v_y is the average velocity of the piston.

The discharge time (τ_{dis}) must allow a sufficient difference in electric field to be maintained between the leading and trailing edges of the piston so that it is pulled through the channel. Within the 1-D model (Eq. (6) and Figs. 10 and 11), this condition appears to be easily met within a wide range of realistic physical parameters (e.g., ϵ , σ , l_y).

As discussed in the next section, circuit theory shows that the recharge time (τ_{rec}) will be longer than the discharge time and should not present an operational problem. Typically, τ_{rec} for p-n diodes of physical dimensions comparable to the *standard device* are $\tau_{rec} \simeq 10^{-7} - 10^{-8}$ sec. However, in order for the electric field in the gap to thermally regenerate enough to maintain force on the piston, the period of oscillation of the piston in the channel (τ_{osc}) must be longer than τ_{rec} , and ideally, much longer. Therefore, for the smooth operation of the motor, the ordering for characteristic time scales should be $\frac{l_y}{v_y} \simeq \tau_{dis} < \tau_{rec} \ll \tau_{osc} \simeq \frac{2L_y}{v_y}$. Since the salient growth and decay rates are exponentials in time, small differences in τ are significant.

3.2 R-C Network

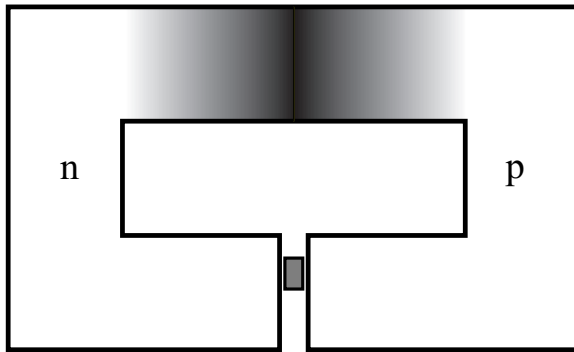
The electrostatic motor (Figs. 9c and 12a) can be modeled as a network of discrete resistors and capacitors (Fig. 12b). The semiconductor capacitor plates are modeled as a distributed network of resistors (R) and their interior surfaces as a sequence of aligned parallel plate capacitors (C). The network is powered by a battery (V_s).

The piston is represented by a resistor and by an accompanying switch. The piston's motion is modeled by the sequential closing and opening of the local switches. As the piston leaves a capacitor _{n} region, a closed switch _{n} opens up, while the next switch _{$n+1$} in line closes, signaling the arrival of the piston. The trailing capacitor recharges while the leading capacitor discharges.

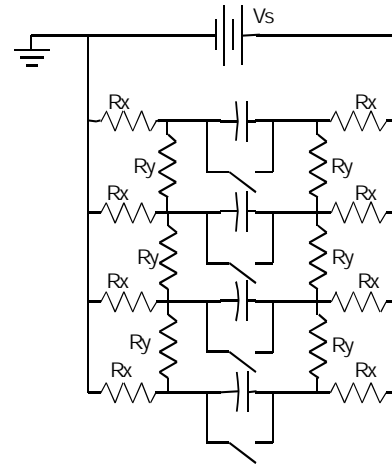
It can be shown from basic circuit theory – and has been confirmed by parametric studies of this system using PSpice network simulations – that the time constant for the discharging capacitor is less than the time constant for the recharging capacitor. As a result, the moving piston always finds itself moving in the direction of more intense electric fields and field gradients. In other words, it perpetually moves forward toward a lower local energy state, riding in a self-induced potential energy trough [39]. In this regard this semiconducting piston acts analogously to the conducting piston in a magnetic rail gun [36] which, by completing the circuit between the gun's two electrified rails, establishes a current and magnetic field by which the resultant Lorentz force on the piston's current drives the piston along the rails. In the present electrostatic case, the piston is propelled forward by the greater $(\mathbf{p} \cdot \nabla)\mathbf{E}$ force on its leading edge. This traveling negative energy pulse, depicted in Fig. 12c, is the sum of the time-varying discharge and recharge energies of local capacitors triggered by the piston; the piston is trapped in and propelled by this pulse.

When the piston reaches the end of the R-C network, where the field ahead has dropped off, but where field behind has regenerated, the piston reverses its motion. As a result, it will move cyclically through the network. It is remarkable that this motion does not require any electronic timing circuitry; instead, the timing is set by the piston itself. As long as it overcomes friction, the piston will run perpetually for the life of the battery.

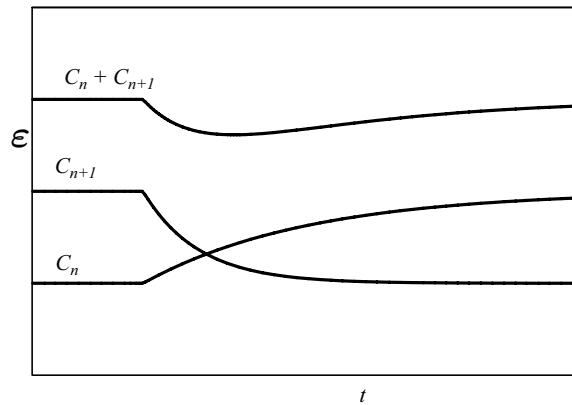
It is important to realize that, as it is now described, the electric field that propels the piston is provided by a battery, so no thermodynamic laws are jeopardized. However, in fact, the origin of the electric field is irrelevant to the operation of the piston; the piston simply responds to it. Via the substitution $V_s \rightarrow V_{bi}$, the piston in Figs. 9 and 12 may now be identified as the semiconductor piston in Case 3 (Fig. 3c). The same



(a) Piston in *standard device*.



(b) Analog resistor-capacitor network model.



(c) Electrostatic energy versus time for sequential firing of two capacitors; traveling negative potential energy pulse evident in $(C_n + C_{n+1})$ curve.

Figure 12: Linear electrostatic motor modeled as a discrete resistor-capacitor network.

physics applies, with the exception that whereas the free energy for the linear electrostatic motor (rail gun) above is supplied by a battery, now it is supplied by the free energy of the thermally-powered p-n depletion region.

3.3 2-D Numerical Model

Essentials of the above 1-D dynamical nonequilibrium model of the linear electrostatic motor are corroborated by the equilibrium solutions of the 2-D model. Figure 13 presents a sequence of 2-D equilibrium solutions simulating aspects of the motion of the piston through the J-II region of the *standard device*. It is strongly emphasized that this is *not* a dynamical simulation in which the piston is modeled as moving; rather, these are quasi-static equilibrium configurations of the system simulated by the Atlas program in which the piston is held at rest at different locations in the J-II region [40], despite implicit force imbalances. Nevertheless, much physics can be inferred by stepping the piston through the channel in this fashion.

In Fig. 13a, the leading edge of the piston is visible above the J-II channel. The electric field is fairly uniform in the gap interior ($E \simeq 7 \times 10^6$ V/m), decreasing in strength at its ends, as expected [41]. As the piston enters the gap, thereby initiating the bridging of the separated n- and p-regions, the electric field strength falls throughout the J-II vacuum and p-n bulk regions, but most strongly near the piston. This substantiates the β term in Eq. (6). The field and field gradients are stronger below the piston (in the direction of implied motion) than above it (outside the channel); as a result, should the piston be free to move, it would be drawn further into the channel. In Fig. 13c, with the piston now squarely within the channel, the electric fields in and near the piston have been reduced by a factor of 3 below pre-insertion values, but they remain larger in the channel ahead of the piston and, therefore, continue to draw it in.

In Fig. 13d, as the piston approaches mid-channel, the field ahead of the piston continues to be more intense than the one behind. At mid-channel, (Fig. 13e), the field is roughly balanced on both sides of the piston. Here, a resting piston would experience roughly no net force, but it would be in the unstable equilibrium position depicted in Fig. 9b. Were it in motion, then it would continue to see stronger fields and field gradients ahead of it than behind it and, thus, would continue to move in the direction of motion. Furthermore, since presumably it has already accelerated to mid-channel from the gap ends, its inertia should carry it past this mid-channel equilibrium point.

Now compare the upper channel in Figs. 13d and e. Notice the field has been partially restored between 13d and 13e after the “passage” of the piston. Finally, in Fig. 13f, the piston has reached the bottom of the channel. As before, the field is locally reduced, but it has regenerated behind. Since the field is now stronger behind the piston, it should exert a net force upward so as to reverse its motion. It is instructive to view this “motion sequence” in reverse, proceeding from 13e→13a so as to appreciate how the piston’s motion can be cyclic. This is most evident perhaps in the inversion symmetry seen between Figs. 13c and 13f.

Figure 14 displays the equilibrium electrostatic potential energies of the *standard device* and *piston* for a sequence of steps through the channel, calculated with the Atlas 2-D simulator. Frames a, b, c, d, e, and f in Fig. 13 correspond to Steps 1, 3, 5, 7, 9 and 13, respectively, in Fig. 14. The total, vacuum, and p-n bulk energies of the *standard device* decrease significantly and symmetrically as the piston enters the channel from either direction and reaches the mid-channel (Step 9). The fractional change in field energy in the vacuum is greater than for the p-n bulk, but the greatest absolute change occurs in the bulk. The electrostatic energy invested in the piston itself is small compared with the bulk and vacuum contributions, similarly as in Fig. 8.

It follows, from the principle of virtual work and from the energy minimum at the center of the channel, that the piston should naturally be drawn toward mid-channel by forces acting inward from the gap openings, in agreement with the electric field values in Fig. 13. The slopes in the energy curves (Fig. 14) are due

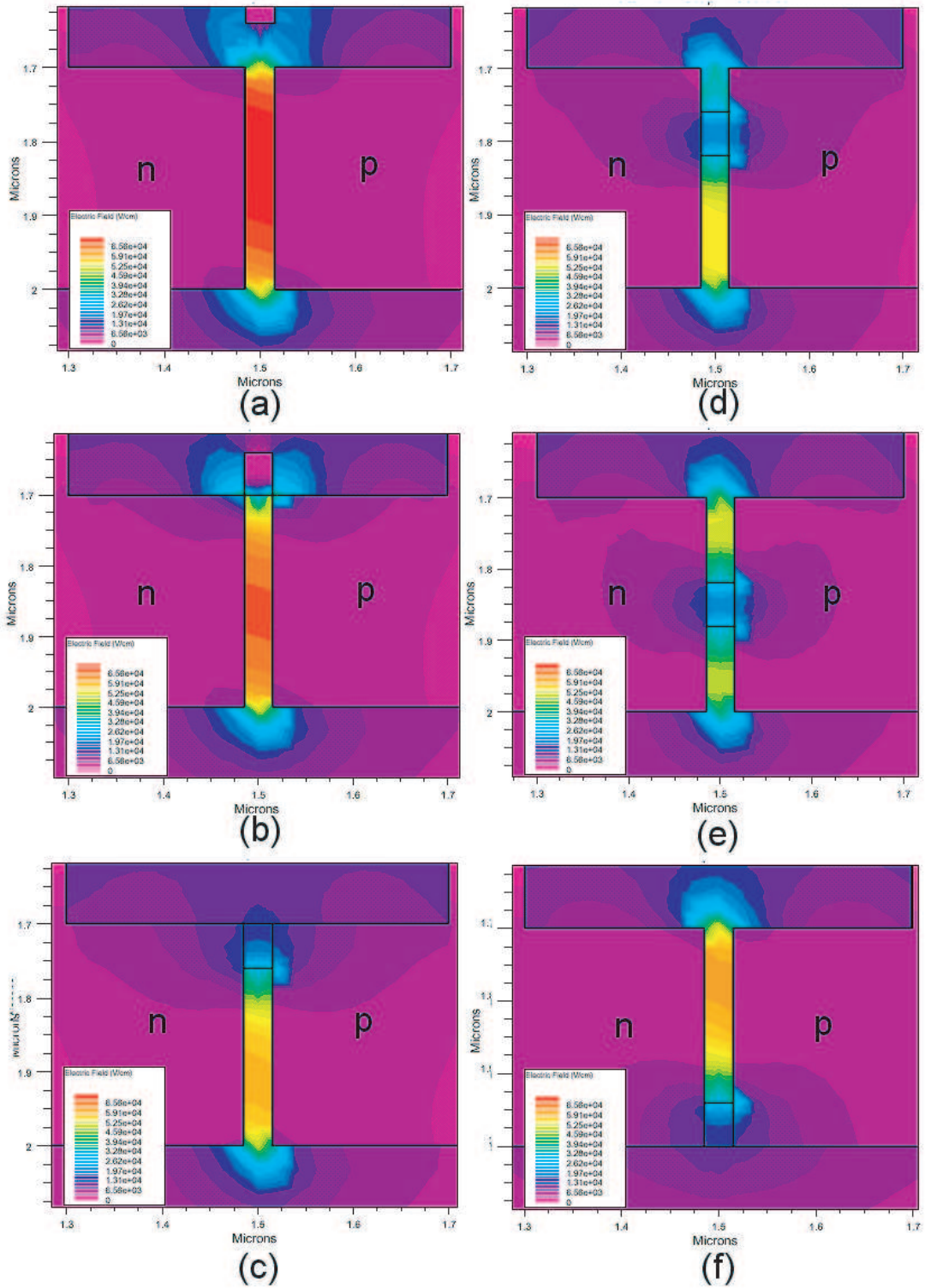


Figure 13: Sequence of 2-D Atlas simulations of electric field for *standard device* with static piston at various locations in J-II channel. (Details in text.)

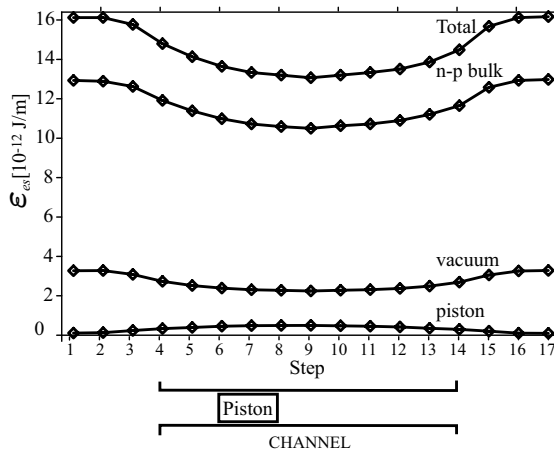


Figure 14: Electrostatic potential energy of *standard device* versus piston position in J-II gap: Total energy, p-n bulk energy, vacuum energy, and piston energy indicated. Piston located at Step 7, corresponding to Fig. 13d.

to edge effects; the energy curve for the case of a very long channel would be nearly flat away from the ends. This does not mean, however, that the piston would not be subject to strong electrostatic forces in the direction of its motion even at mid-channel. Recall that the data in Fig. 14 are equilibrium solutions and assume the piston to be at rest. The energy depression seen in Fig. 14 would occur only locally around the piston and would be spatially asymmetric, with its greatest strength and gradient in the direction of the piston's motion, both as suggested in individual frames of Fig. 13, in Fig. 12c, and in the 1-D analytic model (Sect. 3.1).

The dynamical quantities estimated from the virtual work 1-D model (e.g. force, acceleration) were cross-checked against estimates made using numerical results of the Silvaco 2-D simulator. The simulator gave numerical values of electric field (x -, y - components and total E) with high spatial resolution, from which field gradients could be inferred. From these the $(\mathbf{p} \cdot \nabla)\mathbf{E}$ force on the piston could be estimated. The estimated $\mathbf{p} \cdot \nabla)\mathbf{E}$ forces were in good agreement with the 1-D analytic model. This is encouraging given that the simulator rendered steady-state field values, whereas the system and the 1-D model are inherently time-dependent, due to the piston's motion. In summary, the sequential 2-D numerical simulations (Figs. 13 and 14) support the 1-D nonequilibrium analyses preceding it.

4 Solid State Maxwell Demon

The steady-state operation of this solid-state electrostatic motor constitutes a Maxwell demon; that is, it is a *perpetuum mobile* of the second type. It pits the first law of thermodynamics against the second. If the piston cycles perpetually while under load, performing work, then this energy must come from somewhere. Assuming the first law is absolute, the only possible source of this unlimited energy must be the [infinite] heat bath surrounding the device. Since the device operates in a thermodynamic cycle, heat is transformed solely into work, in violation of the second law. One can summarize how the device transforms heat into work as follows. Electrons and holes are generated thermally in the n- and p-regions throughout the device.

Thermal diffusion of charge carriers at J-I establishes a voltage difference between the regions across the depletion region. This potential drop, also expressed across the narrow J-II gap, results in large electric fields and stored electrostatic potential energy there; this configuration is a high-energy metastable state. The electrostatic potential energy is extracted to perform work by adjusting the J-II boundary conditions (closing the gap). When these boundary conditions are reversed (opening the gap), the same thermal processes cause the system to revert to its original thermodynamic state and the work cycle can be repeated. The net result of the cycle is the transformation of heat (which generates the free charges responsible for the excess electrostatic energy) into work (motion and work of the load-bearing piston). All resolutions commonly applied to second law challenges appear to fail for this one. The reader may refer to Appendix B of Ref. [6] for a compendium of these.

This section addresses the practical details of this demon, paying especial attention to the operational limits imposed by physically realistic parametric values: mass, physical dimensions, electric field, friction, electrical conductivity, characteristic time scales (e.g., τ_{dis} , τ_{rec} , τ_{osc}), and statistical fluctuations. It is found that there exists a broad parameter space at and below the micron-size scale for which a semiconducting piston should be able to overcome realistic levels of friction and load so as to perform work indefinitely, while being driven solely by the thermally-generated electric fields of a p-n junction. It is found that these devices should be able to convert heat energy into work with high instantaneous power densities, perhaps greater than 10^8 W/m³ [42].

Consider the *standard piston* situated in the J-II gap of the *standard device*. As indicated in Fig. 7b, the dopant concentrations $N_A = N_D \equiv N$ are below the crossover density N_{cross} , so one expects a positive energy gain from gap closure. From Fig. 14, the *standard piston* should reside in a potential well approximately 3×10^{-18} J deep. From Figs. 10 and 11, in the frictionless case the piston should experience a maximum acceleration of 10^8 m/sec² and be capable of instantaneous power outputs of 2×10^{-9} W. We will now consider a realistic model for friction.

Let the J-II channel walls be tiled with a thin, low-friction surface such as graphite. Let the outer surfaces of the piston be only partially tiled with a matching low-friction surface such that the contact fraction between the piston and the channel walls (f_c) is small ($0 < f_c \ll 1$). On the other hand, let f_c be sufficiently large that: (i) there are sufficient numbers of atoms projecting out from the piston surfaces in contact with the channel walls to hold and guide the piston; and (ii) there is sufficiently good electrical conduction between the piston and the channel walls that one can use standard Ohmic current rather than quantum mechanical tunneling current to describe the system's electrical behavior [43].

It is well known that, at micron and sub-micron size scales, atomic, ionic, and electrostatic forces (e.g., van der Waals' interactions, induced surface charge, molecular and hydrogen bonding, surface tension) can play dominant roles in system dynamics [44]. In order to minimize friction between the piston and channel walls, f_c should be as small as possible, while at the same time satisfying other practical necessities of the device listed above.

The smallest non-zero coefficients of static and kinetic friction yet measured experimentally are found in nested multi-walled carbon nanotubes (MWNT) [45-48]. Upper-limit values of coefficients of static (s) and kinetic (k) friction have been experimentally measured to be: $\mathcal{F}_s < 2.3 \times 10^{14}$ N/atom = 6.6×10^5 N/m², and $\mathcal{F}_k < 1.5 \times 10^{-14}$ N/atom = 4.3×10^5 N/m². Theoretical arguments suggest true values could be much lower than these. This friction is presumed to arise purely from van der Waals' interactions between the sliding carbon contact surfaces. The friction can be reduced by reducing the contact fraction f_c [49]. Experimental observations suggest that MWNT operate as totally wear-free bearings [45].

The static or kinetic friction $F_{f(s,k)}$ between two surfaces of area A , where normal forces are not imposed and asperities are absent, should scale as: $F_{f(s,k)} = f_c A \mathcal{F}_{(s,k)}$. For the piston in the J-II channel, the acceleration is:

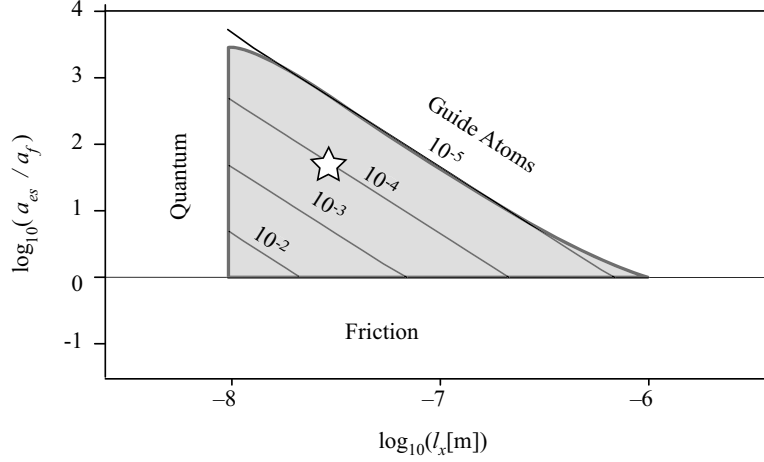


Figure 15: Ratio of piston acceleration to frictional acceleration ($\text{Log}_{10}(\frac{a_{es}}{a_f})$) versus gap width (x_g) with contours of constant f_c indicated. Viability regime delimited by labeled boundary lines. Star indicates location of *standard device*.

$$a_{f(s,k)} = \frac{F_{f(s,k)}}{m} = \frac{f_c A \mathcal{F}_{(s,k)}}{\rho_{Si} l_x l_y l_z} = \frac{2 f_c \mathcal{F}_{(s,k)}}{\rho_{Si} l_x} \quad (7)$$

For the piston to begin moving in the channel the electrostatic acceleration must exceed the static friction:

$$\frac{a_{es}}{a_{f,s}} = \frac{(\epsilon - \epsilon_o) V_{bi}^2 (\alpha_1^2 - \alpha_2^2)}{4 l_x l_y f_c \mathcal{F}_s} > 1 \quad (8)$$

This inequality is the starting point for delimiting a viability regime for the operation of this device. For the *standard piston* in the *standard device* (letting \mathcal{F}_s be the upper-limit value for MWNT [45] and taking $(\alpha_1^2 - \alpha_2^2) \simeq 0.5$), Eq. (8) reduces to:

$$\frac{a_{es}}{a_{f,s}} \simeq (3.2 \times a^{-18}) \frac{1}{l_x^2 f_c} \quad (9)$$

In Fig. 15 is plotted $\text{Log}_{10}(\frac{a_{es}}{a_{f,s}})$ versus l_x for various contours of constant f_c . For $\text{Log}_{10}(\frac{a_{es}}{a_{f,s}}) < 0$, the frictional acceleration exceeds the electrostatic acceleration, so the piston cannot move. This places a lower bound on the viability regime of the *standard device*. Above this bound, the piston can experience sizable accelerations, on the order of $10^7 - 10^8 \text{m/sec}^2$, but these accelerations are still within mechanical strength limits for small structures.

A left-most viability bound for the *standard device* is found by requiring that l_x significantly exceed the size of individual atoms and, preferably, be large enough that the system can be treated by classical, rather than quantum, theory [50]. If the piston thickness l_x is greater than about 50-100 atoms, or about 10^{-8}m , this system should be essentially classical. This criterion sets the left-most bound of the viability regime in Fig. 15. The last bound is set by restricting f_c such that some reasonable minimum number of atoms act as guide surfaces between the piston and the channel walls. Choosing 10 atoms/piston face as sufficient,

the sigmoidal right-top viability bound is determined. This bound can later be modified to satisfy electrical conductivity constraints.

The viability regime has been delimited using realistic, but conservative, choices for the system parameters. More liberal choices (e.g., letting $\mathcal{F}_s \rightarrow \mathcal{F}_k$ or $(\alpha_1^2 - \alpha_2^2) = 0.8$) would expand the regime somewhat. Even as it stands, however, the viability regime for the electrostatic motor spans two orders of magnitude in size ($10^{-8}\text{m} \leq l_x \leq 10^{-6}\text{m}$) and over three orders of magnitude in $\frac{a_{es}}{a_{f,s}}$.

Several observations can be made from Fig. 15:

- a) The spontaneous acceleration of the piston by self-generated fields appears possible only for micron and sub-micron pistons. This is especially evident in Eq. (6) where $a_{es} \sim \frac{1}{l_x^3}$. Given the severe physical and mechanical requirements for positive acceleration against friction (See Eqs. 8 and 9), it is not surprising that this phenomenon has not been discovered accidentally.
- b) a_{es} can exceed a_f by more than 3 orders of magnitude, thus allowing significant loading of the piston with which to perform work.
- c) More frictional contact surfaces appear feasible (up to 10^3 times more frictional than MWNT), without precluding piston motion or loading.

The magnitude of the piston's acceleration ($a_p = a_{es} - a_f$) can be calculated, including friction, using Eqs. (5 - 7). For the *standard device*, using graphitic surfaces and assuming $f_c = 10^{-4}$ (corresponding to 1.7×10^6 atoms on each piston face), one finds $a_f = 1.9 \times 10^6 \text{ m/sec}^2$, $a_{es} = 6.7 \times 10^7 \text{ m/sec}^2$, and $a_p = 6.5 \times 10^7 \text{ m/sec}^2$. The average velocity during a piston stroke is roughly $v_y \simeq \sqrt{2L_y a_p} \simeq 2\text{m/s}$. The oscillation period of the piston in the channel is $\tau_{osc} = (\frac{2L_y}{v_y}) \simeq 2 \times 10^{-7}\text{sec}$; the oscillation frequency is $f_{osc} = \tau_{osc}^{-1} \simeq 5 \times 10^6\text{Hz}$. τ_{osc} is significantly longer than the typical inverse slew rates for p-n transistors of comparable physical dimensions ($\tau_{dis} \leq \tau_{rec} \sim \tau_{trans} \sim 10^{-8} - 10^{-7}\text{sec} \ll \tau_{osc} \simeq 2 \times 10^{-7}\text{sec}$); therefore, the electric field in the wake of the piston traversing the channel can recharge before the piston's return. On the other hand, given a typical piston velocity and length ($v_y \simeq 2\text{m/sec}$, $l_y \simeq 6 \times 10^{-8}\text{m}$), these field decay rates are sufficiently high for the electric field in the channel walls to decay along the length of the piston ($\tau_{dis} \simeq \frac{l_y}{v_y} \sim 3 \times 10^{-8}\text{sec}$) so as to admit significant difference in the magnitude of the electric field between the leading and trailing edge of the piston; therefore, the apriori estimate of $((\alpha_1^2 - \alpha_2^2) = 0.5)$ is plausible. A similar conclusion is supported by evaluation of the exponential decay model (in Eq. (6)). Overall, the time scale ordering developed earlier ($\tau_{dis} \leq \tau_{rec} \ll \tau_{osc}$) is reasonably well satisfied.

The current flow through the piston and the time-changing electric field (displacement current) resulting from the piston's motion will generate a magnetic field (Ampere-Maxwell law), which itself will be time-changing as the piston moves, thereby inducing a secondary electric field (Faraday's law). The magnitudes and dynamical effects of these induced fields can be shown to be insignificant to the overall operation of the device.

The viability regime depicted in Fig. 15 is favorable to Ohmic treatment of the piston and channel. The piston acts as a sliding electrical resistor – essentially a motor brush – between the positive polarity n-region and the negative polarity p-region, as depicted in Fig. 16. The piston's electrical resistance can be written as

$$R_{piston} = R_b + 2R_c = \frac{1}{l_y l_z} \left[\frac{x_g - 2l_c}{\sigma_b} + \frac{2l_c}{f_c \sigma_c} \right] \simeq \frac{1}{l_y l_z} \left[\frac{l_x}{\sigma_b} + \frac{2l_c}{f_c \sigma_c} \right] \quad (10)$$

where $R_{b(c)}[\Omega]$ is the electrical resistance of the piston bulk (contacts); $\sigma_{b(c)}[(\Omega\text{m})^{-1}]$ is the electrical conductivity of the bulk (contact) material; and l_c is the x -length of the contacts. It is assumed that $l_c \ll l_x \simeq x_g$. The values of the l_c and f_c are both small and offset one another, while σ_c can in principle be varied over many orders of magnitude [51] such that R_c can be made negligible compared with R_b . Consider, for example, the *standard device* with a silicon piston lined with graphite, operating with the following parameters:

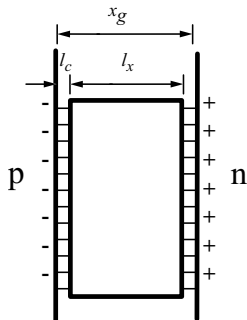


Figure 16: Physical dimensions of *standard piston*.

$l_x = 300\text{\AA}$, $l_y = 600\text{\AA}$, $l_z = 10^4\text{\AA}$, $l_c = 5\text{\AA}$, $\sigma_b = 10\sigma_{Si} = 4 \times 10^{-3}(\Omega m)^{-1}$, $\sigma_c = \sigma_{graphite} = 7.1 \times 10^4(\Omega m)^{-1}$, and $f_c = 10^{-4}$. With these parameters, one has from Eqs. (6-10): $R_b \simeq 10^8\Omega \gg R_c = 2.5 \times 10^3\Omega$ and ($a_{es} = 6.7 \times 10^7\text{m/sec}^2$) $\dot{}$ ($a_p = 6.5 \times 10^7\text{m/sec}^2$)

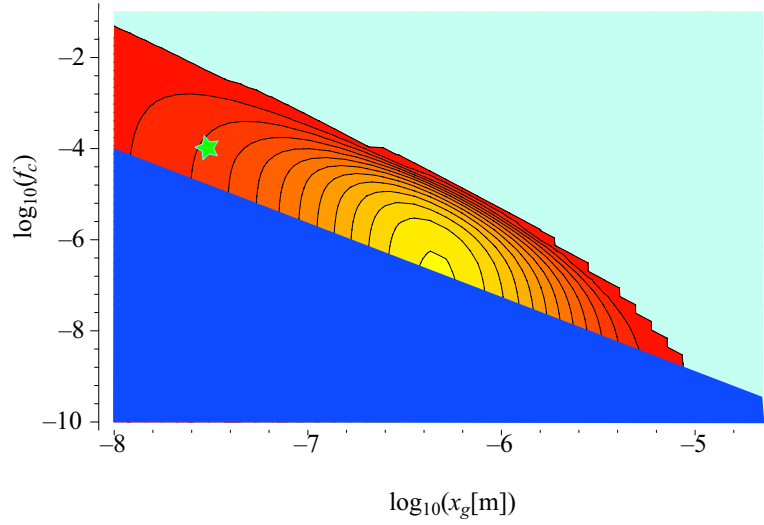
$\gg (a_{f,s} = 1.9 \times 10^6\text{m/sec}^2)$ $\dot{}$ ($a_{f,k} = 1.2 \times 10^6\text{m/sec}^2$).

Ohmic losses for this system, concentrated in the piston region, can be engineered to be insignificant. If the piston is composed of undoped silicon, it should decrease the maximum theoretical power production of the *standard device* by about 10%, however, if it is even lightly doped (e.g., $N \sim 10^{19}\text{m}^{-3}$), then Ohmic dissipation can be several orders of magnitude less than power production, thus should be operationally negligible. Ohmic heating of the piston can likewise be shown to be negligible.

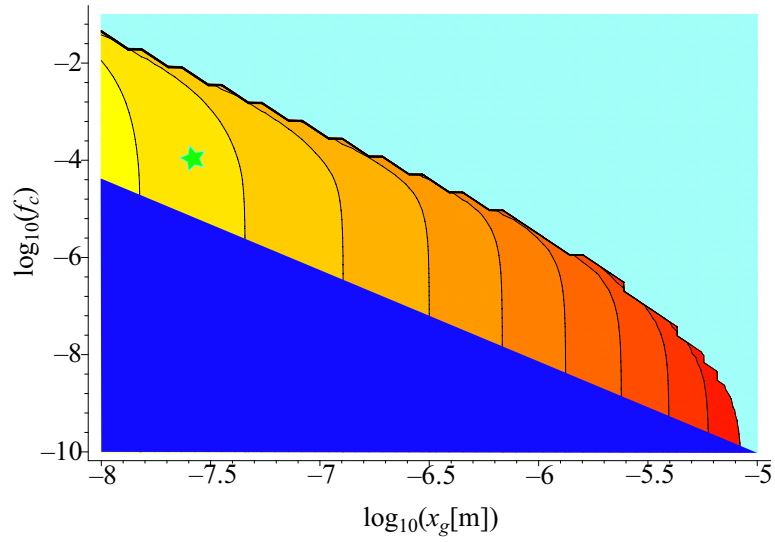
For objects in this size range, the effect of statistical fluctuations should be considered, especially since they have been the foil of many past challenges [26]. Earlier analysis indicates the *standard device* can be modeled as an R-C network, so it is appropriate to consider fluctuations in electronic charge. Charge is also naturally salient since it is through charge-induced electric fields that the system is powered. Spectral analysis in the spirit of the Nyquist and Wiener-Khintchine theorems [52] allows one to write the rms charge fluctuation for a resistor capacitor system as $\sqrt{\langle \Delta Q^2 \rangle} = \Delta Q_{rms} \sim \sqrt{4RC^2kT\Delta f}$, where C is capacitance of the J-II region and Δf is the spectral width of the fluctuations measured. Taking characteristic values for the *standard device* ($R = 10^9\Omega$, $C = \frac{\epsilon_0 L_y l_z}{l_x} = 10^{-16}\text{F}$, $\Delta f \sim f_{osc} \simeq 5 \times 10^6\text{Hz}$, $T = 300\text{K}$), one obtains $\Delta Q_{rms} \simeq 2$ electronic charges. Since the total charge in the *standard device's* J-II region is found to be $Q_{total} \simeq 330q$, one expects less than one percent statistical fluctuation in electronic charge over the entire J-II channel capacitor during a piston's oscillation period. Since the fractional statistical fluctuation is much less than the fractional change in charge due to electrical operation of the piston itself ($0.01 \simeq \frac{\Delta Q_{rms}}{\Delta Q_{total}} \ll \frac{\Delta Q_{op}}{\Delta Q_{total}} \simeq 0.4$), by this measure, statistical fluctuations should not play a primary role in the operation of the *standard device*.

Assuming that a_{es} is constant in magnitude and that $a_{es} \gg a_f$, the average power per cycle can be shown to be $\langle P_{sd} \rangle = m_{piston}(2a_p^3 L_y)^{1/2} \simeq 2 \times 10^{-9}\text{W}$, where $m_{piston} = \rho_{Si} l_x l_y l_z$ is the mass of the piston. The average power densities for the *standard device* are, therefore, $\mathcal{P}_{sd} \sim 2 \times 10^9\text{Wm}^{-3}$. The *standard device* appears capable of producing significant output power and power densities in the presence of realistic levels of friction, while satisfying the conditions for classical electrical conductivity, providing substantial numbers of guide/contact atoms, and overcoming statistical fluctuations.

In Fig. 17, power (W) and power density (Wm^{-3}) are explored for a range of device sizes, scaled in direct physical proportion to the standard device (i.e., $l_y = 2l_x$, $L_y = 5l_y$, $l_z = 33.3l_x$, etc.). The other physical specifications of the *standard device* are retained (i.e., silicon matrix, $N_A = N_D = 10^{21}\text{m}^{-3}$, etc.). The



(a) Maximum power output versus gap width (x_g) and contact fraction (f_c). Contours vary linearly from 10^{-9} W/device (red) to 1.2×10^{-8} W/device (yellow).



(b) Power density (Wm^{-3}) versus x_g and f_c . Contours vary logarithmically from 10^1 Wm^{-3} (red) to 10^{10} Wm^{-3} (yellow). Star indicates location of *standard device*.

Figure 17: Device power and power density over range of devices size-scaled to *standard device*.

previously discussed viability bounds (Fig. 15) are still enforced. In Figure 17a, the maxima of the power curves (Fig. 11c) are calculated over an extended viability regime (as in Fig. 15) and plotted versus l_x and f_c . Power contours extend linearly in value from a maximum of 1.2×10^{-8} W/device (yellow, center) down to 1×10^{-9} W/device (red). The star indicates the location of the *standard device*. The device with the largest output power ($x_g \simeq 4.5 \times 10^{-7}$ m, $P = 1.2 \times 10^{-8}$ W) is roughly 15 times larger than the *standard device*, but produces only roughly 10 times more power even though it occupies more than 3300 times greater volume. The largest viable device within the present constraints ($x_g \simeq 10^{-5}$ m) has physical dimensions visible to the naked eye ($x_{dev} \simeq 3.3 \times 10^{-4}$ m); 2-D numerical energy calculations indicate it should perform analogously to the *standard device*.

Perhaps a more meaningful figure of merit than maximum power per device (Fig. 17a) is maximum power density (Wm^{-3}). It is a better indicator of how rapidly thermal energy can be transformed into work by a given volume of working substance; thus, it is a better measure of how significantly this device challenges the second law. In Fig. 17b, maximum power density (Wm^{-3}) is presented for a range of devices versus f_c and x_g , scaled as before in direct physical proportion to the *standard device*. Whereas in Fig. 17a the contour values vary linearly with adjacent contours, in Fig. 17b they vary logarithmically in value from 10^{10}Wm^{-3} (left-most, yellow) to 10Wm^{-3} (right-most, red). Again, the *standard device* is located by the star. The greatest power density obtains for small devices, while the greatest unit power obtains for larger devices.

The parameter space available for this device (spanned by x_g , x_{dev} , N_A , N_D , T , etc.) is far greater than can be explored in this paper and little attempt has been made to optimize the performance of the *standard device*. Nonetheless, it appears the theoretical instantaneous power densities achievable by it are sizable. To put this in perspective, one cubic meter of *standard devices* (amounting to 10^{18} in number) could, in principle, convert thermal energy into work with instantaneous power output on par with the output of a modern-day nuclear power plant; or, in 1 second, produce the work equivalent of the explosive yield of 500 kg of high-explosive. This, of course, is only *instantaneous* power density since, were the device to convert thermal energy into work at this rate without compensatory heat influx from the surroundings, the device would cool at an unsustainably fast rate of about 100 K/sec.

We note that Fig. 17 is created under the generalized premises of the 1-D model. The piston moves in an infinitely long channel, travels at the peak of its power-velocity curve (Fig. 11c) and converts into work all of the electric field energy ($E = 2 \times 10^8$ V/m (Fig. 6)) it encounters. The 2-D model, which supports more modest electric fields (7×10^6 V/m (Fig. 6)) and a piston that oscillates in a finite channel at sub-optimal speeds, predicts power densities an order of magnitude lower than the 1-D model. Should the device design be optimized, it is likely that the maximum achievable power density for the electrostatic motor might fall somewhere between the two.

More advanced designs for the motor can be envisioned. For example, the linear *standard device* could be circularized. This rotary motor would consist of concentric cylinders of n- and p-regions (the stator) joined at their base (to create a depletion region) and having a gap between them in which a multi-piston rotor runs. Multiple rotor pistons could be yoked together so as to balance radial forces and torques. In the limit of large radius, the rotor pistons would move in what is essentially a linear track, so the above discussion for linear motors should apply. The rotor pistons would be driven by the local electric field energy. If they are spaced sufficiently far apart azimuthally, then the field in the wake of a given piston could thermally regenerate in time to power the advancing piston.

The rotor assembly would not require vertical support since the gap electric field maximum would reside near its vertical center, in which case $(\mathbf{p} \cdot \nabla)\mathbf{E}$ forces would naturally guide and levitate the rotor near mid-gap. Analytical estimates indicate this alignment force would outstrip gravity by several orders of magnitude. In fact, if a bare rotor assembly were simply brought into the vicinity of an empty stator, the electrostatic forces would be such that the rotary motor should self-assemble and begin to run spontaneously.

Prospects are good for laboratory construction and testing of this solid state Maxwell demon in the near future. Present-day micro- and nano-manufacturing techniques are adequate to construct the necessary structures [27-29, 53-55], however, the art of surface finishing, which is crucial to reducing friction, may not yet be adequate. State-of-the-art molecular beam epitaxy can reliably deposit layers to monolayer precision, but control of surface states is still problematic. Self-assembly of the requisite surfaces is plausible [56,57]. Large scale biotic systems (e.g., DNA, microtubules [58]) are well-known to self-assemble with atomic precision, as are abiotic ones (e.g., carbon nanotubes [47,48]). Molecularly catalysed construction (e.g., RNA to protein transcription inside ribosomes [58]) is accomplished with atomic precision. Scanning tunneling microscopes have also been used to assemble complex systems atom by atom [59]. In light of these accomplishments, it seems plausible that experimental tests of this solid-state challenge to the second law may be on the horizon [60].

References

1. D.P. Sheehan, *Phys. Plasmas* **2**, 1893 (1995).
2. D.P. Sheehan, *Phys. Plasmas* **3**, 104 (1996).
3. D.P. Sheehan and J.D. Means, *Phys. Plasmas* **5**, 2469 (1998).
4. D.P. Sheehan, *Phys. Rev.* **E 57**, 6660 (1998).
5. D.P. Sheehan, *Phys. Lett. A* **280**, 185 (2001).
6. D.P. Sheehan, J. Glick and J.D. Means, *Found. Phys.* **30**, 1227 (2000).
7. D.P. Sheehan, J. Glick, T. Duncan, J.A. Langton, M.J. Gagliardi and R. Tobe, *Found. Phys.* **32**, 441 (2002).
8. D.P. Sheehan, *J. Sci. Explor.* **12**, 303 (1998).
9. A.E. Allahverdyan and Th. M. Nieuwenhuizen, *Phys. Rev. Lett.* **85**, 1799 (2000).
10. A.E. Allahverdyan and Th. M. Nieuwenhuizen, *Phys. Rev.* **E**, (In press) (2002).
11. V. Capek O. and Frege, *Czech. J. Phys.* **50**, 405 (2000).
12. V. Capek and T. Mancal, *Europhys. Lett.* **48**, 365 (1999).
13. V. Capek, *Phys. Rev.* **E 57**, 3846 (1998).
14. V. Capek, *J. Phys. A: Math. Gen* **30**, 5245 (1997).
15. V. Capek and D.P. Sheehan, *Physica A* **304**, 461 (2002).
16. V. Capek and O. Frege, *Czech. J. Phys.* (in press) (2002).
17. L.G.M. Gordon, *Found. Phys.* **13**, 989 (1983).
18. L.G.M. Gordon, *Found. Phys.* **11**, 103 (1981).
19. A.V. Nikulov, *Phys. Rev.* **B 64**, 012505 (2001).
20. A.V. Nikulov and I.N. Zhilyaev, *J. Low Temp. Phys.* **112**, 227 (1998).
21. V. Capek and D.P. Sheehan, *Challenges to the Second Law of Thermodynamics*, in *Fundamental Theories of Physics Series* (Kluwer Academic, Amsterdam, due 2003).
22. First International Conference on Quantum Limits to the Second Law, San Diego, July, 2002.
23. J.C. Maxwell, letter to P.G. Tait. 11 December 1867, in *Life and Work of Peter Guthrie Tait*, C.G. Knott, ed. (Cambridge University Press, London, 1911), pp. 213-215.
24. J.C. Maxwell, *Theory of Heat* (Longmans & Green, London, 1871), Chap. 12.
25. H. Whiting, *Science* **6**, 83 (1885).

26. H.S. Leff and A.F. Rex, *Maxwell's Demon Entropy, Information, Computing* (Princeton University Press, Princeton, 1990).
27. W. Trimmer, ed., *Micromechanics and MEMS: Classic and seminal papers to 1990* (IEEE Press, New York 1997).
28. M.C. Roco, R.S. Williams and P. Alivisatos, eds., *Nanotechnology research directions: IWGN workshop report* (Kluwer Academic, Dordrecht 2000).
29. E. Meyer and R.M. Overney, K Dransfeld, T. and Gyalog, *Nanoscience* (World Scientific, Singapore 1998) Chpt. 3,5.
30. J.S. Yuan and J.J. Liou, *Semiconductor device physics* (Plenum Press, New York 1998).
31. G.W. Neudeck, *Vol. II: The pn junction diode 2nd edition*, in *Modular series on solid state devices*, R.F. Pierret and G.W. Neudeck, editors. (Addison-Wesley, Reading 1989).
32. Mid-channel is defined as the geometric center of the channel, midway in the x-direction between the channel walls ($\frac{x_a}{2}$) and midway in the y-direction along the channel length, ($\frac{L_y}{2}$).
33. The 2-D simulation results are truncated below 100\AA because the Atlas simulator does not allow reliable construction below this scale length; the 1-D model is truncated below 200\AA where it predicts field strengths above the dielectric strength of silicon ($E_{max} \simeq 3 \times 10^7$ V/m).
34. A number of energy extraction schemes were considered – ranging from insertion of silicon wedge switch into trapezoidal J-II gap, to resonant electro-elastic oscillation of the entire J-II gap region, to Faraday transformer induction coupling transient magnetic fields during J-II gap closure.
35. D.J. Griffiths, *Introduction to Electrodynamics* (Prentice Hall, Upper-Saddle River 1999), pp. 194-96.
36. R.A. Serway and R.J. Beichner, *Physics for Scientists and Engineers 5th Ed.* (Saunders College, Fort Worth, 2000), pg. 975.
37. If the piston were to scrape charge off the plates, then it might make a single pass through the channel, but since there can be no recharging of the plates (they are insulators), the piston would not cycle. This is an uninteresting case.
38. a_{es} in Eq. (6) is a transcendental function of v_y so piston dynamics are nonlinear, and even more so if the friction or load is a function of position or velocity.
39. The traveling piston can also be viewed as the material equivalent of an electrical pulse propagating through a resistive-capacitive transmission line.
40. Reliable simulators of the full, time-dependent electromagnetic, thermodynamic, and transport equations appropriate for this system are not currently available.
41. The small horizontal mirror asymmetry in the field can be traced to physical/geometric asymmetry between the device interior and exterior, above and below the gap. The vertical mirror asymmetry through the gap middle is due to the differences in physical properties of electrons and holes.
42. The parameters for the *standard device* have not been optimized for power production or efficiency; they are meant to be merely representative.

43. Physical estimates indicate electron tunneling alone may be sufficient to support device operation in the absence of Ohmic current, but this is beyond the scope of this paper.
44. D. Bishop, P. Gammel and C.R. Giles, C.R., *Physics Today* **54**, 38 (2001).
45. J. Cumings and A. Zettl, *Science* **289**, 602 (2000).
46. Y. Min-Feng, B.I. Yakobson, and R.S. Ruoff, *J. Phys. Chem.* **104**, 8764 (2000).
47. M.S. Dresselhaus, G. Dresselhaus, and P. Avouris, eds., *Carbon nanotubes – synthesis, structure, properties and applications* (Springer-Verlag, Berlin 2001).
48. P.J.F. Harris, *Carbon nanotubes and related structures*, (Cambridge University Press, Cambridge 1999).
49. Low f_c is commonly assumed for proposed micro- and nanoscale bearings.
50. Quantum effects do not appear to preclude the challenge, but they are beyond the scope of this discussion.
51. Almost no other common physical variable varies over as many orders of magnitude as electrical conductivity. Between copper and quartz it varies 24 orders of magnitude. This variability allows for wide tuning of the piston dynamics.
52. R.K. Pathria, *Statistical Mechanics* (Pergamon, Oxford 1972) pp. 467-74.
53. S.Y. Chou, P.R. Krauss and P.J. Renstrom, *Science* **272**, 85 (1996).
54. S. Matsui, *Proc. IEEE* **85**, 629 (1997).
55. J. Sone, *Nanotechnology* **10**, 135 (1999).
56. S.I. Stupp, et al. *Science* **276**, 384 (1997).
57. S.Y. Chou and L. Zhuang, *J. Vac. Sci. Technol. B* **17**, 3197 (1999).
58. W.M. Becker, J.B. Reece, J.B. and M.F. Poenie, *The World of the Cell* (Benjamin/Cummings, Menlo Park 1996), Chpt. 1,20.
59. C.J. Chen, *Introduction to scanning tunneling microscopy* (Oxford University, New York 1993).
60. The authors predict that a laboratory test will be feasible within 5 years.

Acknowledgements: This work was supported by a USD Faculty Research grant and DOE grant ER54544. The authors thank Dr. T. Schubert of the USD Electrical Engineering Department for valuable assistance. We also thank the three referees for their prompt, insightful, and detailed criticisms, which significantly strengthened this work.